Toward liquid cell quantum sensing: Ytterbium complexes with ultra-narrow absorption

Ashley J. Shin,[1*] Changling Zhao,[2*] Yi Shen,[1*] Claire E. Dickerson,[1*] Barry Li,[1] Daniel Bím,[1] Timothy L. Atallah,[1,3] Paul H. Oyala,[4] Lianne K. Alson,[1] Anastassia N. Alexandrova,[1] Paula L. Diaconescu,[1] Wesley C. Campbell,[2] and Justin R. Caram[1†]

[1]*Department of Chemistry and Biochemistry, University of California, Los Angeles, California, 90095, USA*
[2]*Department of Physics and Astronomy, University of California, Los Angeles, California, 90095, USA*
[3]*Department of Chemistry and Biochemistry, Denison University, Granville, Ohio, 43023, USA*
[4]*Division of Chemistry and Chemical Engineering, California Institute of Technology, Pasadena, California, 91103 USA*

**These authors contributed equally to this work*
[†]jcaram@chem.ucla.edu

In quantum technology (such as atomic vapor cells used in precision magnetometry), the energetic disorder induced by a fluctuating liquid environment acts in direct opposition to the precise control required for coherence-based sensing. Overcoming fluctuations requires a protected quantum subspace that only weakly interacts with the local environment. Herein, we report a ferrocene-supported ytterbium complex ((thiolfan)YbCl(THF), thiolfan = 1,1′-bis(2,4-di-*tert*-butyl-6-thiomethylenephenoxy)ferrocene) that exhibits an extraordinarily narrow absorption linewidth in solution at room temperature with a full-width at half-maximum of 0.625 ± 0.006 meV. A detailed spectroscopic analysis allows us to assign all near infrared (NIR) transitions to atom-centered *f-f* transitions, protected from the solvent environment. A combination of density functional theory and multireference methods match experimental transition energies and oscillator strengths, illustrating the role of spin-orbit coupling and asymmetric ligand field in enhancing absorption and pointing toward molecular design principles that create well-protected yet observable electronic transitions in lanthanide complexes. Narrow linewidths allow for a demonstration of extremely low-field magnetic circular dichroism at room temperature, employed to sense and image magnetic fields, down to Earth scale. We term this system an ‘atom-like molecular sensor’ (ALMS), and propose approaches to improve its performance.

TOC Graphic

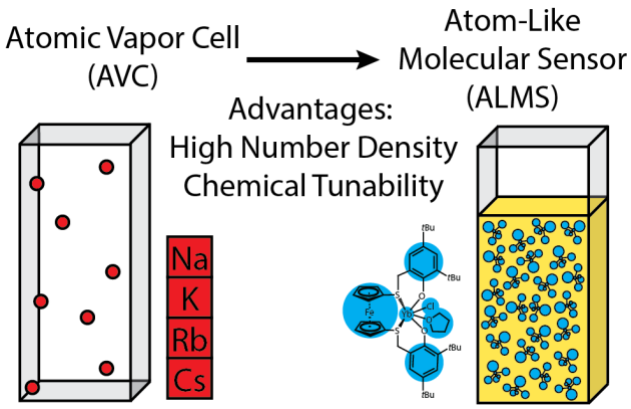
Atomic Vapor Cell
(AVC)
Atom-Like
Molecular Sensor
(ALMS)
Advantages:
High Number Density
Chemical Tunability
Na
K
Rb
Cs

Atomic vapor cells (AVCs) are one of the most sensitive and widely deployed methods of detecting electromagnetic fields with applications ranging from astronomy, medicine, geophysical surveys, explosives detection, to remote sensing.[1,2] AVCs are typically derived from K, Cs, or Rb in a sealed container, where laser excitation is used to drive an 'ns' to '(n+1)*p*' transition. By monitoring the absorption/fluorescence of these gas-phase alkali atoms, AVC magnetometers have reached extraordinary sub-femtotesla sensitivity in a relatively compact form factor.[3,4] Furthermore, combining microwave excitation and optical pump lasers allows for the preparation of collective quantum states of these systems that can be used for quantum measurement.[3,5,6]

The established limit of AVC sensitivity for magnetic fields is set by the spin-projection noise:

$$\Delta B \approx \frac{1}{g\mu_B}\frac{\hbar}{\sqrt{N\tau T}}$$

Where ΔB is the uncertainty in the measured magnetic field, g is the ground state Landé factor, μ_B is the Bohr magneton, $\hbar$ is the Planck's constant, N is the number of atoms, τ is the coherence time, and T is the measurement duration.[1] In AVCs, a higher N would improve sensitivity, but in practice it is offset by lower τ due to increased collision-based dephasing.[1,4,7–10] A liquid analogue to an AVC, e.g. an atomic-like molecular sensor (ALMS), would utilize atomic-like transitions while minimizing drawbacks by accessing much higher number densities. If narrow linewidths can be retained in solution, the number density/pathlength limits of AVCs could be overcome.

To explore this capability, we chose the *f*-centered transitions in trivalent lanthanide complexes— often referred to as 'atom-like'—as a potential testbed for the applicability of atomic physics technologies in condensed-phase chemistry. We focus on Yb^{3+}, noting that the $4f^{13}$ electron configuration allows for well-protected, electronic transitions between a small manifold of spin-orbit electron configurations. In the gas phase, these transitions are parity-forbidden (interacting

only through magnetic dipole), but the ligand environment allows us to open small electric dipole transitions among *f*-electron configurations creating atom-centered transitions with non-negligible oscillator strengths.[11,12] As a result, they display near infrared absorption bands, which retain extremely narrow yet measurable linewidths even in condensed phase environments.[13,14] Solubilization allows for a high number density of these species in a set volume, reaching upwards of 10^{19} molecules per cm^3 (i.e., 10 mM), a value eight orders of magnitude greater than the average density of their AVC counterparts.[15–18]

In this paper, we demonstrate an unprecedented ultranarrow (<1 meV) linewidth achieved in a room-temperature, molecular lanthanide system—a suggestive first step to liquid-based quantum sensing. Optical and magnetic spectroscopy with detailed electronic structure calculations allow us to assign these spectral features and point to design principles for "near-atomic" localized transitions in the metal center of the molecule. We show that a suitably narrow linewidth allows for liquid-based optical measurements of magnetic fields through direct transmission of circularly polarized light, down to the Earth's magnetic field (~0.25 G),[19] paving the way toward a novel liquid-based magnetometry method. Our results represent first steps toward liquid systems which can be analogized to an atomic vapor cell technology.

Results and discussion

Synthesis of Yb Complexes. The Yb(III) complex, $[(\text{thiolfan})\text{YbCl}]_2$ (thiolfan = 1,1′-bis(2,4-di-*tert*-butyl-6-thiomethylenephenoxy)ferrocene), was synthesized by deprotonating H_2(thiolfan), followed by a reaction with $YbCl_3(THF)_3$ (THF = tetrahydrofuran) at -78 °C (Supplementary Information Section I-A,B). The solid-state molecular structure revealed a dinuclear compound, $[(\text{thiolfan})\text{YbCl}]_2$, where the sample was crystallized out of toluene and has two ytterbium centers bridged by two chlorides (fig. S1). The compound was fully characterized by nuclear magnetic resonance spectroscopy and elemental analysis (figs. S2-4). However, we note that the spectral measurements in the following sections were performed after dissolving the sample in THF or 2-MeTHF (2-Methyltetrahydrofuran), in which the compound exists as a monomer. The monomer sample is coordinated to the solvent molecules, specifically with THF in the solution phase and 2-MeTHF in the glass phase, which was confirmed by diffusion ordered spectroscopy (DOSY), electron paramagnetic resonance (EPR), and UV-Vis spectroscopy measurements (Supplementary Section I-E).

The preference for the dimeric form in solid and monomeric form in solution is confirmed by direct measurement of the sample's magnetic susceptibility. The magnetic properties were investigated using a superconducting quantum interference device (SQUID) and the Evans method.[20] A magnetic susceptibility value of $\chi_m T = 4.77\ emu \cdot K/mol$ was obtained for the solid sample from direct current susceptibility measurements at room temperature after a diamagnetic correction. This in line with the reported $\chi_m T = 5.14\ emu \cdot K/mol$ for two Yb(III) centers ($^2F_{7/2}$, $g_J = 8/7$) (further details in Supplementary Section I-F). The paramagnetic properties of the monomer, (thiolfan)YbCl(THF), were evaluated in THF-d_8 revealing $\chi_m T = 2.47\ emu \cdot K/mol$

at room temperature, in line with the reported value for a single Yb(III) center ($\chi_m T = 2.57\ emu \cdot K/mol$), further confirming the presence of monomeric Yb(III) in solution.

To investigate the relationship between the structural and spectral properties of this class of Yb(III) compounds, two derivatives of (thiolfan)YbCl(THF), **1**, were synthesized: (thiolfan*)YbCl(THF), **2**, thiolfan* = 1,1′-bis(2,4-di-*tert*-butyl-6-thiophenol)ferrocene, and (thiolfan)Yb[N(SiMe$_3$)$_2$], **3**. They were made separately for comparison by modifying the supporting ligand and exchanging the chloride with an amide, respectively. Spectroscopic data presented in this study pertains to Yb samples in THF, unless otherwise noted.

Electronic spectroscopy. We measured the broadband electronic absorption spectrum of (thiolfan)YbCl(THF) (fig. 1a) using a conventional UV-Vis spectrometer (figs. 1b-c). We observe

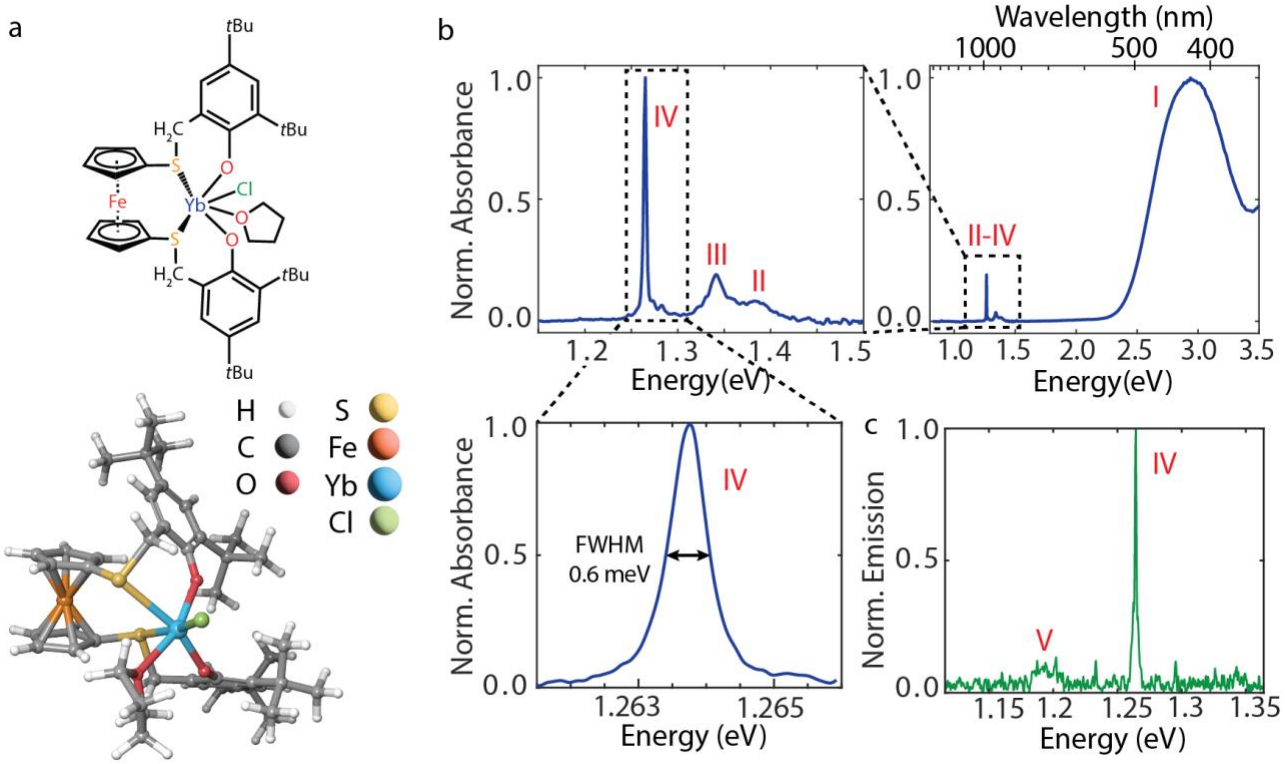

Figure 1. **Optical characterization of (thiolfan)YbCl(THF).** (a) Drawing (top) and DFT-optimized geometry (bottom) of (thiolfan)YbCl(THF). (b) Wide-field absorption spectrum with zoomed in absorption spectrum around the Yb features, showing a high-resolution absorption scan of the Yb transition with the highest oscillator strength around 980 nm or 1.262 eV in the bottom left. (c) Normalized emission spectrum, obtained through Fourier-transform spectroscopy.

several features: a broad ligand absorption band (**I**) in the visible range around 400-600 nm (fig. S11), several weakly absorbing transitions (**II** and **III**) from 880-950 nm, and the transition of primary interest: the strongly absorbing, ultranarrow transition (**IV**) at 980 nm. As evident in the small spread of transitions **II**-**IV**, lanthanide complexes possess strong spin-orbit coupling (~1 eV) and much smaller ligand field splitting (~10-100 meV) than typical transition metal complexes.[21,22] Our primary focus is on the narrow transition denoted **IV**, which shares a similar energy gap to that of the gas phase Yb^{3+} ion (i.e., arising almost entirely from spin-orbit splitting). Conventional UV-Vis spectrometers lack the resolution necessary to quantify sub 1 meV linewidths in the near infrared. Therefore, we utilize a narrowband, continuous-wave Ti:sapphire laser to scan the transmission (fig. 1d; Supplementary section II-B for methods).

The resulting high-resolution spectrum of **IV** fits best to a Lorentzian function with a center energy of 1.2637 eV with a full width at half maximum (FWHM) of 0.625±0.006 meV. Exciting at the ligand absorption band (425 nm), we also recorded the fluorescence spectra using a home-built high-resolution Fourier spectrometer (fig. 1e). The emission is collected in an all-reflective off-axis parabolic epifluorescence set up, after which it goes through a Mach-Zender interferometer and towards superconducting nanowire single photon detectors.[23] We note two emission bands, one which overlaps nearly perfectly with **IV** observed in absorption, and another band, **V**, separated by 80 meV. **IV** shows negligible Stokes shift between absorption and emission, consistent with minimal vibronic coupling.

To investigate the intrinsic linewidth of transition **IV**, we collected absorption as a function of temperature down to 7 K (fig. 2a-b). The feature remains unimodal at cryogenic temperatures, with a slight broadening and blue shift in peak energy as the temperature increases to 300 K (full temperature range shown in (fig. S13). It should be noted that the sample was frozen in a glass-forming solvent (2-MeTHF), and not crystallized out of solution. Thus, the spectra in fig. 2a reflect the optical behavior of the sample in disordered glass at varying temperatures, therefore more closely reflecting its behavior dissolved in solution, as opposed to a solid or crystal. The peak frequency and the FWHM starts to increase near 100 K, corresponding to the glass transition of the solvent and its concurrent decrease in density.[24] The fact that cryogenic temperatures did not resolve any underlying features suggests that **IV** is dominated by a single inhomogeneously

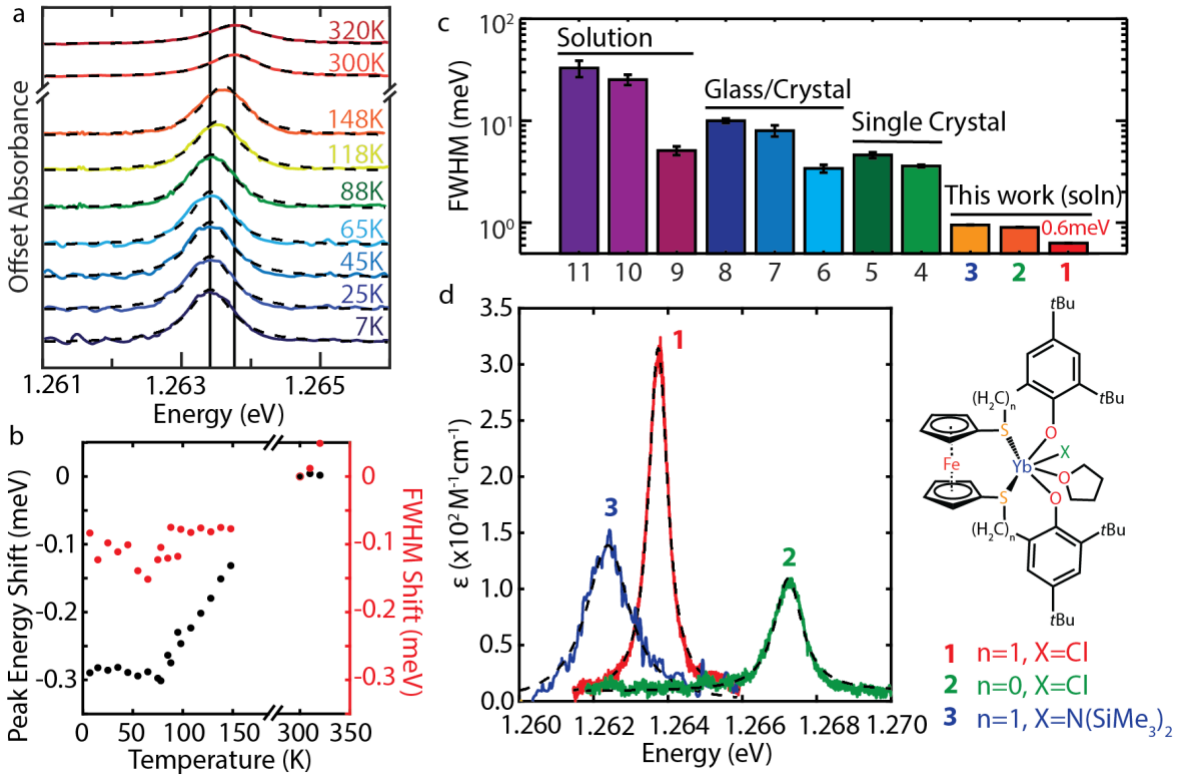

Figure 2. **Investigating linewidth broadening mechanisms.** a) Temperature-dependent absorption scans, using liquid N_2 and He for cooling. The dashed lines indicate the corresponding Lorentzian fits. Solid vertical lines are a visual guide to emphasize the shift in peak center. b) FWHM and transition energy offsets from corresponding room temperature values and their temperature trend. Error bars were too small and are shown in SI fig. S13. c) FWHM comparison to other Yb(III) complexes (references shown in SI Section II-D). d) Drawing of compounds with different ligand designs and their corresponding absorption peaks.

broadened transition, brought on by different solvation environments (rather than vibrational coupling). That is, individual chromophores may have slightly different geometries and thus varying transition energies. We further hypothesize that the intrinsic homogenous linewidth of individual chromophores is most likely narrower than the feature shown in fig. 2a.

(thiolfan)YbCl(THF) displays a narrower room temperature solution linewidth compared to many similar systems in the condensed phase, optical cavities, and cryogenic temperatures (fig. 2c #1-8; references in tab. S1).[25–32] Our central hypothesis for the correlation between molecular structure and the ultra-narrow linewidth is that the rigidity of the ferrocene backbone in the supporting ligand sphere minimize inhomogeneous broadening and *f*/*d* orbital coupling, respectively. For example, Yb(trensal) (where H_3(trensal) is 2,2',2"-tris(salicylideneimino)triethylamine) is a compound with a high degree of magnetic anisotropy and well-defined optical features that shows a linewidth of 4.6 meV (fig. 2a #6), roughly an order of magnitude broader than (thiolfan)YbCl(THF).[27] Contrary to our system, Yb(trensal) shows many absorption features assigned to other spin-orbit transitions and vibrations, and a large apparent Stokes shift, suggesting a more mixed and "molecular" electronic structure in comparison. Even Yb^{3+} doped crystals at 4 K show a larger linewidth of 3.6 meV (fig. 2a #7), almost 6 times broader than (thiolfan)YbCl(THF), attributed to inhomogeneous crystal environments and phonon coupling.[28,33]

We investigated the relationship between this ultranarrow linewidth and molecular geometry by synthesizing two variants of (thiolfan)YbCl(THF) with slightly different ligand environments (fig. 2d), a variant with one fewer carbon connecting the ferrocene and phenoxy moieties (fig. 2d: **2**) and another variant by replacing -Cl with $-N(SiMe_3)_2$ (fig. 2d: **3**). A high-resolution scan of the transmission of the three variants indicates that the linewidth of transition

IV is preserved, likely because the rigidity of the ferrocene backbone provides protection of the radiative transition **IV** from other sources of line broadening. The amide variant **3** has a FWHM of 0.947 ± 0.005 meV, while **2** has a FWHM of 0.902 ± 0.007 meV, which are both comparable to the 0.625 meV linewidth of **1**. Although the exact broadening mechanism is unknown, the slight increase in linewidth is mostly likely due to the shorter carbon bridge of **2** changing metal-ligand coupling, and the strong ligand field of the amide group in **3** contributing to the inhomogeneous broadening of the metal transition. The important observation, however, is that all three ytterbium complexes display near record linewidths in solution, despite shifts in the primary transition energy that can be attributed to slight deviations in the coordination geometry. Therefore, the original thiolfan ligand preserves the narrowest Yb^{3+} transition linewidth, while minimizing the ligand effects relative to the ground spin-orbit transition (**IV**).

Electronic structure analysis with multireference calculations. The isolated Yb^{3+} ion possesses seven degenerate states arising from orbitals of the 4*f* shell with 13 valence electrons. Large electronic spin-orbit coupling separates the 4*f* states into spin-orbit states, creating the primary optical NIR transition from the 8-state $^2F_{7/2}$ to the 6-state $^2F_{5/2}$ manifolds.[14] In a molecular framework, each spin-orbit manifold is further split due to the ligand-field contributions, giving rise to the individual electronic transitions **II-V** (fig. 3a). Crystal field analysis of transition energies and oscillator strengths (described in SI section III-A) prompted us to assess the degree of molecular/atomic character of this transition using multireference electronic structure theory (see the SI section III-B). Our calculations show that **IV** is primarily composed of states with ~99% 4*f* character, with the ground and excited states containing mixtures of several 4*f* orbitals. To demonstrate, a visual guide, shown in figure 3b, captures the primary states that contribute to the ground and excited state wavefunctions, although we note that these pictures do not reflect the

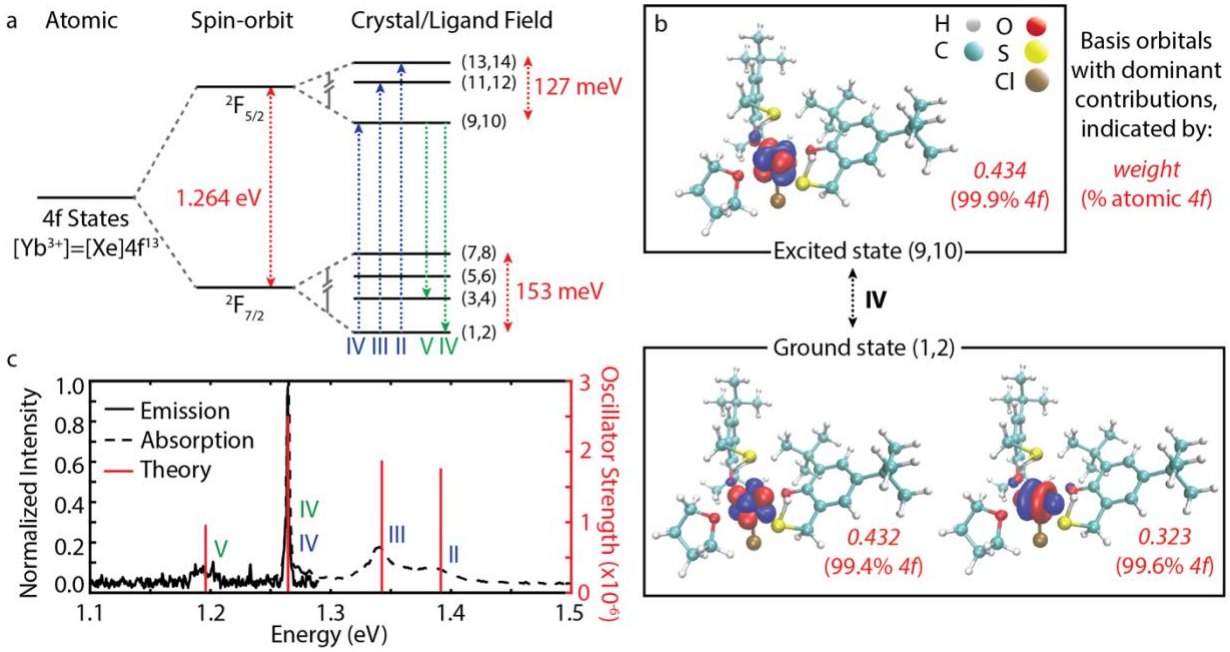

Figure 3. a) Electronic structure diagram showing the incorporation of spin-orbit and ligand field effects on the Yb^{3+} atomic orbitals, calculated with CASSCF/CASPT2/RASSI-SOC level of theory. b) Visualization of the CASSCF basis orbitals that have dominant contribution(s) to the molecular orbitals involved with transition **IV**, demonstrating the "atom-like" properties. c) Comparison between emission/absorption data and the transition energies and oscillator strength calculated by multireference calculations.

overall multireference nature of the molecular orbitals (full set of complete active space, CAS, orbitals shown in tabs. S3 and S4).

We find that inclusion of the virtual Yb 5*d* orbitals into the '13 electrons in 12 orbitals' active space (i.e., 7 x Yb(4*f*) + 5 x Yb(5*d*)) is critical for obtaining the transition energies and oscillator strengths, in agreement with experiment, and in accordance with the Judd-Ofelt theory (fig 3c).[34] Primarily, we attribute the enhanced oscillator strengths to an increased mixing between the 4*f* and 5*d* states through spin-orbit coupling, loosening the Laporte selection rules to allow E1 transitions (tab. S5). Additionally, the 5*d* virtual orbitals mix with virtual ligand orbitals, lowering them in energy and further enhancing oscillator strength. By incorporating the virtual 5*d* orbitals in the active space, we observe a slight change from the purely 4*f* atomic orbitals to molecular orbitals containing small contributions from the ligands (tab. S6). Due to lowering the symmetry of 4*f* states, the increased ligand character may also be responsible for an enhancement in the calculated oscillator strengths in transitions **II, III,** and **IV**. Also, the atom-like characteristic of the molecular orbitals is further confirmed by the agreement among calculated g factors for the ground and excited states ($g_g = 7.89$ and $g_e = 4.26$), the expected g factors of gas-phase Yb^{3+} ($g_g = 8$ and $g_e = 4.28$), and experimentally obtained values ($g_g = 7.486 \pm 0.008$ and $g_e = 3.2 \pm 0.2$; further details of the full g-matrix in SI Section III-C). Altogether, we describe the transitions **II-V** from fig. 3c as dominated by Yb 4*f* orbitals. Since the strength of spin-orbit coupling fundamentally contrasts with the covalency of the metal-ligand bond, we speculate both 4*f*/5*d* and 5*d*/ligand effects must be balanced in the system, and the transition energies and intensities can thus be influenced by the geometry and the nature of the ligand, as observed for different ligand designs (fig. 2d).

Detecting AC and DC magnetic fields. We decided to leverage the extraordinarily narrow linewidth of (thiolfan)YbCl(THF), and its open-shell character to detect magnetic fields. We first performed magnetic circular dichroism (MCD) measurements to study spin characteristics. MCD measures the differential absorption of σ^+ and σ^- circularly polarized light induced in a sample under a strong magnetic field that is oriented parallel to the light propagation.[35] Typically, resolving these shifts requires a superconducting magnet, cryogenic temperatures, and lock-in detection.[36] In contrast, we easily measure these shifts using a permanent rare-earth magnet set under the sample at room temperature. With a 0.38 T field, we induce a 23 GHz (0.011 meV) shift in **IV** between right- and left-hand circularly polarized excitations, corresponding to Zeeman

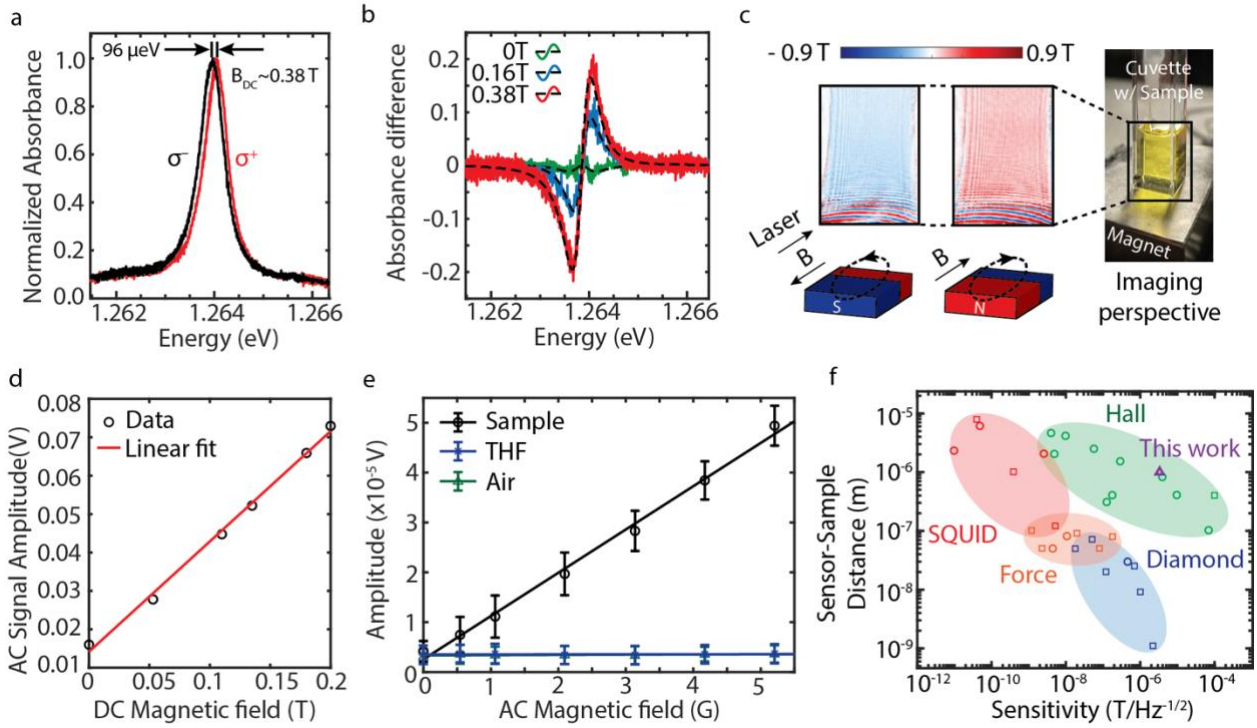

Figure 4. a) Room temperature Zeeman splitting under a static magnetic field of 0.38 T. b) Differential absorbance of left and right circularly polarized light under varying DC field strengths. c) MCD imaging of the magnetic field generated by a permanent magnet in two different orientations. d) Amplitude of the oscillating transmitted light intensity measured with a static magnetic field of 0-0.2 T. e) Increase of frequency modulation signal with the amplitude of the applied AC magnetic field in the presence of (thiolfan)YbCl(THF). f) Compilation of sensitivity values of other spin-based magnetometry imaging methods, as it compares to our work, plotted against the "closest" approach of the sensor. SQUID: superconducting quantum interference device. Hall: Hall effect magnetometer. Force: magnetic resonance force microscopy. Diamond: nitrogen-vacancy (NV) center in diamond magnetometry. This plot was adapted with permission from Dr. Patrick Appel.

transitions of the ground state (fig. 4a). We observe a linear correlation between the magnetic field strength and Zeeman splitting by changing the distance between the static magnet and the sample (fig. S15). From the linear correlation of the Zeeman splitting with the static magnetic field, we can extract the effective transition magnetic moment as $(2.2 \pm 0.1)\mu_B$. Finally, the subtraction between the σ^+ and σ^- transitions produces the MCD signals, which vary in intensity with the varying magnetic field strength as expected (fig. 4b).

Using this MCD signal, we demonstrate three different schemes of magnetic sensing. First, we imaged a DC magnetic field at room temperature (fig. 4c). We can visualize the magnetic field generated by the permanent magnet below the sample cuvette with a defocused laser beam and capture the brightness of each pixel with a camera. Since the transmitted circularly polarized light varies with the strength of the magnetic field, we can extrapolate to a magnetic field map, both in intensity and relative direction. The sensitivity of this measurement depends on the uncertainty of the g factor and the resolution of the absorption measurement, leading to a sensitivity of 0.05 T (500 G) with this MCD setup (SI Section IV-B). This imaging can be dynamic, and we show a video of a spinning magnet influencing transmission in Supplementary Video.

Second, we directly measured a DC magnetic field by modulating the polarization of the laser beam at a set frequency (experimental setup in SI Section IV-C). To change the frequency rapidly, we use two acoustic optical modulators, which are driven with different radio frequencies offset by Δf. By combining the two beams together, we create a beam that has oscillating polarizations at frequency Δf. With the presence of a static magnetic field, the transmitted light intensity will also be modulated at Δf, corresponding to the sample's MCD response. At Δf = 100 kHz, we can examine how the amplitude of the transmitted light changes with the static magnetic

field (fig. 4d). We observe the expected linear trend, confirming the capability of this sample to measure static magnetic fields down to a 0.025 T (250 G) difference.

Third, we directly measured an AC magnetic field. We applied a small AC magnetic field (0-5 G at $f_{AC} = 1$ kHz) by adding a Helmholtz coil (SI Section IV-D) to give rise to two more sidebands at frequency $\Delta f \pm f_{AC}$. This signal is measured by a spectrum analyzer, where the sideband peak heights increase with the amplitude of the applied AC magnetic field. The (thiolfan)YbCl(THF) solution shows a monotonically increasing linear trend with the AC magnetic field, whereas the THF solvent and air show no dependence on the magnetic field (fig. 4e). With this method, we can measure AC magnetic fields at 1 kHz down to 0.5 G, which is the scale of the Earth's magnetic field (signal over time shown in fig. S19). Even though these measurements are performed with a room temperature solution, we can achieve a sensitivity of 3.33 μT $\text{Hz}^{-\frac{1}{2}}$.

Comparison to other technologies. There are several important figures of merit in comparing ALMS to other EM sensing technologies—sensitivity, frequency range, and distance from sample. The most important figure of merit is magnetic field sensitivity, which describes the smallest magnetic field that can be detected within a given measurement time. For (thiolfan)YbCl(THF), the sensitivity is governed by the absorption change upon applying a magnetic field, where the most drastic response comes with the steep slopes in the absorption feature. We estimate that our limit in sensitivity is set by the signal-to-noise difference in transmission, where our best resolution comes from the measurement of a small AC magnetic field with 3.33 μT $\text{Hz}^{-\frac{1}{2}}$ sensitivity. The second figure of merit is the frequency at which these signals can be measured. We measured both DC and higher frequency field modulation up to 1 kHz but have not fully characterized the highest frequency possible to measure. We hypothesize it is likely limited by the excited state lifetime of

the system, which is comparable to other Yb(III) complexes (μs to ms). The third figure of merit is the distance at which a magnetic field can be measured, namely the sensor-sample distance. Broadly speaking, the sensor-sample distance represents the effective geometry of a given magnetic sensor. In the context of nanoscale imaging, where magnetometers are used to detect single spin fields, it is crucial that the magnetic field sensor can capture the dipole field, which decreases with the cubed distance. Here, systems with high number densities of magnetically sensitive molecules may provide an advantage. For example, (thiolfan)YbCl(THF) can be concentrated to give an optical density of 1 in a thin 0.2 mm path length cuvette, effectively providing a sensor to sample distance that is considerably shorter than current AVC technologies.

We note that real quantum sensing technologies operate through modulation of ground-state quantum coherences, prepared through optical and microwave pumping, and readout through changes in absorption, polarization, or fluorescence intensity. Besides AVCs, other spin-based magnetometers include nitrogen vacancies in diamond and color centers in crystal environments, both of which are also enabled by optical state preparation of pure quantum states that enable extraordinary sensitivity.[37, 38] Compact designs of AVCs that are widely used in miniature circuits demonstrate an optimal sensitivity of 50 p T $Hz^{-\frac{1}{2}}$ with the most sensitive atomic optical magnetometer exceeding a 10^{-15} T $Hz^{-\frac{1}{2}}$ sensitivity.[1,4,39] The typical sensitivities of magnetic sensing based on single nitrogen vacancy in diamond range from tens of μT $Hz^{-\frac{1}{2}}$ for DC fields to tens of nT $Hz^{-\frac{1}{2}}$ for AC fields.[40] To be competitive with the sensitivities of these devices would require a state preparation and readout of spin superpositions in the electronic ground state that has yet to be shown in a liquid or glass environment. Nevertheless, a simple MCD-based

magnetometry method with (thiolfan)YbCl(THF) puts us at a comparable sensitivity to other known spin-based magnetometers, such as Hall-effect sensors, as shown in fig. 4e.[41,42]

Using MCD as a magnetic contrast approach, we determined that the mathematical limit to the sensitivity of an MCD-based method can be approximated as:

$$\Delta OD \approx \frac{g_{eff}}{\Gamma^2}$$

where the sensitivity of the absorption measurement is proportional to the g_{eff} factor of the driven transition and is inversely proportional to the square of the linewidth Γ (see derivation in SI Section IV-E). This indicates that for transitions with the same oscillator strength, narrowing the linewidth by half will increase the sensitivity by a factor of four, motivating the need for further chemical insight into synthesis and post-synthesis methods that narrow optical transitions.

Conclusion

(thiolfan)YbCl(THF) shows an extraordinarily narrow $^2F_{7/2}$ to $^2F_{5/2}$ lanthanide centered optical transition in solution at room temperature. While the design principles for such a narrow transition will require further investigation, crucial orbital mixing between the *d* and *f* orbitals of Yb and further mixing with the ligand orbitals lead to a non-zero oscillator strength for the observed transition. In parallel, the rigidity and asymmetry afforded by the supporting ligand assist in concentrating the minimal oscillator strength to an ultranarrow transition. This suggests that fine tuning the asymmetric structural components may become a primary design consideration in developing new ALMS systems. Further theoretical, synthetic, and spectroscopic work will help elucidate the tradeoffs between ligand rigidity, orbital mixing, covalency, and solvation environment. In summary, we demonstrate an immediate application of Yb complexes for an

MCD-based measurement and imaging of relatively weak magnetic fields. We achieve sufficient sensitivity by leveraging the large number density afforded by direct solvation of the complex. For further work, we hypothesize that investigation of quantum state preparation and readout of (thiolfan)YbCl(THF) will lead to higher sensitivities in analogy to AVCs, paving the way towards lanthanide complexes in precision quantum sensing.

Online content

Supplementary video – MCD Imaging

References

1. Budker, D. & Romalis, M. Optical magnetometry. *Nat. Phys.* 3, 227–234 (2007).
2. Shah, V., Knappe, S., Schwindt, P. D. D. & Kitching, J. Sub pico-tesla atomic magnetometry with a microfabricated vapour cell. *Nat. Photonics* 1, 649–652 (2007).
3. Degen, C. L., Reinhard, F. & Cappellaro, P. Quantum sensing. *Rev. Mod. Phys.* 89, 035002 (2017).
4. Kominis, I. K., Kornack, T. W., Allred, J. C. & Romalis, M. V. A sub femto-tesla multichannel atomic magnetometer. *Nature.* 422, 596–599 (2003).
5. Kitching, J., Knappe, S. & Donley, E. A. Atomic Sensors - A Review. *IEEE Sens. J.* 11, 1749-1757 (2011).
6. Savukov, I. M. & Romalis, M. V. NMR Detection with an Atomic Magnetometer. *Phy. Rev. Lett.* 94, 123001 (2005).
7. Allred, J. C., Lyman, R. N., Kornack, T. W. & Romalis, M. V. High-sensitivity atomic magnetometer unaffected by spin-exchange relaxation. *Phys. Rev. Lett.* 89, 1308011–1308014 (2002).
8. Budker, D., Kimball, D. F., Rochester, S. M., Yashchuk, V. V. & Zolotorev, M. Sensitive magnetometry based on nonlinear magneto-optical rotation. *Phys. Rev. A.* 62, 043403 (2000).
9. Seltzer, S. J. & Romalis, M. V. Unshielded three-axis vector operation of a spin-exchange-relaxation-free atomic magnetometer. *Appl. Phys. Lett.* 85, 4804 (2004).
10. Kitching, J. Chip-scale atomic devices. *Appl. Phys. Rev.* 5, 31302 (2018).
11. Parker, D., Suturina, E. A., Kuprov, I. & Chilton, N. F. How the Ligand Field in Lanthanide Coordination Complexes Determines Magnetic Susceptibility Anisotropy, Paramagnetic NMR Shift, and Relaxation Behavior. *Acc. Chem. Res.* 53, 1520–1534 (2020).
12. Buono-core, G. E., Li, H. & Marciniak, B. Quenching of excited states by lanthanide ions and chelates in solution. *Coord. Chem. Rev.* 99, 55–87 (1990).
13. An, J., Shade, C. M., Chengelis-Czegan, D. A., ephane Petoud, S. & Rosi, N. L. Zinc-Adeninate Metal-Organic Framework for Aqueous Encapsulation and Sensitization of Near-infrared and Visible Emitting Lanthanide Cations. *J. Am. Chem. Soc.* 133, 1220–1223 (2011).
14. di Bari, L., Pintacuda, G. & Salvadori, P. Stereochemistry and Near-Infrared Circular Dichroism of a Chiral Yb Complex. *J. Am. Chem. Soc.* 122, 5557–5562 (2000).
15. Wang, H., Gould, P. L. & Stwalley, W. C. Photoassociative spectroscopy of ultracold 39K atoms in a high-density vapor-cell magneto-optical trap. *Phys. Rev. A.* 53, R1216(R) (1996).
16. Sushkov, A. O. & Budker, D. Production of long-lived atomic vapor inside high-density buffer gas. *Phys. Rev. A.* 77, 042707 (2008).

17. Schempp, H. et al. Full counting statistics of laser excited Rydberg aggregates in a one-dimensional geometry. *Phys. Rev. Lett.* 112, 013002 (2014).
18. Malossi, N. et al. Full counting statistics and phase diagram of a dissipative rydberg gas. *Phys. Rev. Lett.* 113, 023006 (2014).
19. Geomagnetism Magnetic Field Calculators. https://www.ngdc.noaa.gov/geomag/calculators/magcalc.shtml#igrfwmm.
20. Evans, D. F. The Determination of the Pararnagnetic Susceptibility of Substances in Solution by Nuclear Magnetic Resonance. *J. Chem. Soc.* 1959, 2003-2005 (1958).
21. Dey, A., Kalita, P. & Chandrasekhar, V. Lanthanide(III)-Based Single-Ion Magnets. *ACS Omega.* 3, 9462–9475 (2018).
22. Flanagan, B. M., Bernhardt, P. v., Krausz, E. R., Lüthi, S. R. & Riley, M. J. A ligand-field analysis of the trensal (h3trensal = 2,2′,2″-tris(salicylideneimino)triethylamine) ligand. An application of the angular overlap model to lanthanides. *Inorg. Chem.* 41, 5024–5033 (2002).
23. Atallah, T. L. et al. Decay-Associated Fourier Spectroscopy: Visible to Shortwave Infrared Time-Resolved Photoluminescence Spectra. *J. Phys. Chem. A.* 123, 6792–6798 (2019).
24. Deetz, J. D. et al. Liquid-to-glass transition of tetrahydrofuran and 2-methyltetrahydrofuran. *Chinese Physics B* 21, 086402 (2012).
25. Yb:YAG. *Crytur* https://www.crytur.com/materials/ybyag/ (2022).
26. Atzori, M. et al. Helicene-Based Ligands Enable Strong Magneto-Chiral Dichroism in a Chiral Ytterbium Complex. *J. Am. Chem. Soc.* 143, 2671–2675 (2021).
27. Pedersen, K. S. et al. Design of Single-Molecule Magnets: Insufficiency of the Anisotropy Barrier as the Sole Criterion. *Inorg. Chem.* 54, 7600–7606 (2015).
28. Kirmiz, A., Saiki, D. J. & Augustine, M. P. Cavity ring-down observation of Yb^{3+} optical absorption in room temperature solution. *Spectrochim. Acta. A. Mol. Biomol. Spectrosc.* 75, 1211–1217 (2010).
29. Wang, L. et al. Ytterbium-doped phosphate glass single mode photonic crystal fiber with all solid structure. *Opt. Mater. Express.* 5, 742 (2015).
30. Zhang, W. et al. Yb-doped silica glass and photonic crystal fiber based on laser sintering technology. *Laser. Phys.* 26, 035801 (2016).
31. Gorczyński, A. et al. New field-induced single ion magnets based on prolate Er(iii) and Yb(iii) ions: tuning the energy barrier U_{eff} by the choice of counterions within an N_3-tridentate Schiff-base scaffold. *Inorg. Chem. Front.* 5, 605–618 (2018).
32. Suyver, J. F. et al. Novel materials doped with trivalent lanthanides and transition metal ions showing near-infrared to visible photon upconversion. *Opt. Mater.* 27, 1111–1130 (2005).
33. Petit, P. O., Petit, J., Goldner, P. & Viana, B. Inhomogeneous broadening of optical transitions in Yb:$CaYAlO_4$. *Opt. Mater.* 30, 1093–1097 (2008).
34. Walsh, B. M. Judd-Ofelt theory: Principles and Practices. *Advances in Spectroscopy for Lasers and Sensing.* 403–433 (2006).
35. Stephens, P. J. Theory of Magnetic Circular Dichroism. *J. Chem. Phys.* 52, 3489 (2003).

36. Dunbar, T. D., Warren, W. L., Tuttle, B. A., Randall, C. A. & Tsur, Y. Electron Paramagnetic Resonance Investigations of Lanthanide-Doped Barium Titanate: Dopant Site Occupancy. *J. Phys. Chem. B.* 108, 908–917 (2004).
37. Jacques, V. et al. Magnetometry with nitrogen-vacancy defects in diamond. *Rep. Prog. Phys.* 77, 056503 (2014).
38. Castelletto, S. & Boretti, A. Silicon carbide color centers for quantum applications. *J. Phys. Photonics.* 2, 022001 (2020).
39. Schwindt, P. D. D. et al. Chip-scale atomic magnetometer. *Appl. Phys. Lett.* 85, 6409 (2004).
40. Casola, F., van der Sar, T. & Yacoby, A. Probing condensed matter physics with magnetometry based on nitrogen-vacancy centres in diamond. *Nat. Rev. Mat.* 3, 1–13 (2018).
41. Degen, C. Microscopy with single spins. *Nat. Nanotechnol.* 3, 643–644 (2008).
42. Appel, P. *Scanning Nanomagnetometry: Probing Magnetism with Single Spins in Diamond*. http://edoc.unibas.ch (2017).

Acknowledgements

We acknowledge the support of the NSF CCI Phase I grant 2221453. The synthetic and basic characterization experiments were supported by the NSF Grant CHE-1809116 to PLD. AJS was funded by an NSF NRT AIF-Q Fellowship from grant 2125924. YS is grateful for an INFEWS fellowship (NSF DGE-1735325). CED would like to acknowledge support from NSF DGE-2034835. Work in the WCC lab was supported by AFOSR under contract no. FA9550-20-1-0323 and the NSF under grant no. OMA-2016245. The Caltech EPR facility acknowledges support from the Beckman Institute and the Dow Next Generation Educator Fund.

Author contributions

AJS and CZ performed the optical characterization and MCD measurements. YS synthesized and characterized the samples, as well as contributed to the writing of those sections. CED, BL, and DB performed calculations and contributed to the analysis and writing of the results. TLA contributed to the fluorescence measurement. LKA contributed to the figure editing and writing of the manuscript. ANA, PLD, WCC, and JRC supervised the investigation and contributed to the writing. AJS wrote the original draft and all authors discussed the results and commented on the manuscript.

Competing interests

The authors declare no competing interests.

Additional information

Supplementary information. The online version contains supplementary material.

Correspondence and requests for materials should be addressed to Justin R. Caram.